Numerical study on the fluid-structure interaction and species transport in a piezoresistive microcantilever-based biosensor

J. Pérez-Barrera† and S. Piedra*

SECIHTI-Centro de Ingeniería y Desarrollo Industrial,
Av. Playa Pie de la Cuesta No. 702, Santiago de Querétaro, 76125, Querétaro, México.
†*Current address: Departamento de Termofluidos, Facultad de Ingeniería-UNAM,*
Circuito Escolar, Ciudad Universitaria, 04510, CDMX, México.
**e-mail: saul.piedra@cidesi.edu.mx*

D. Díaz Alonso and D. A. Fernández-Benavides

Centro de Ingeniería y Desarrollo Industrial,
Av. Playa Pie de la Cuesta No. 702, Santiago de Querétaro, 76125, Querétaro, México.

Received 17 June 2024; accepted 21 January 2025

In this study, we present numerical simulations of the flow-induced deflection of a microcantilever beam and the distribution of a passive analyte inside a microfluidic cell for a piezoresistive biosensor. The numerical implementation was validated using semi-analytical models and previously reported experimental measurements. The primary objective of the study is to understand the impact of the flow on the cantilever's behavior and use this knowledge in the decision-making process for a microfluidic cell design for a piezoresistive biosensor. To accomplish this, the results for three different inlet/outlet configurations allow us to describe the dynamics of the fluid-structure interaction, finding that, for small times, the flow is symmetrical around the microcantilever. As time passes, two vortices surround the microcantilever, resulting in an asymmetric flow distribution. Throughout the entire range of analyzed inlet flow rates, it is evident that the inlet/outlet configuration significantly influences the deflection and stress sustained by the cantilever. Similarly, these configurations affect how the concentration of an analyte sample distributes on the detecting surface. The in-depth understanding of the flow dynamics within the microfluidic cell and its effect on the cantilever, as provided by the simulations, can be used to propose design recommendations aimed at reducing the noise due to the flow, ultimately achieving high sensitivity in these types of devices.

Keywords: Fluid-structure interaction; computational fluid dynamics; piezoresistive cantilever; biosensor design.

DOI: https://doi.org/10.31349/RevMexFis.71.040601

1. Introduction

Micromechanical cantilever-based transducers have emerged as a promising technology for developing biosensors due to their high sensitivity to small surface changes resulting from immunological reactions between analytes and bioreceptors [1,2]. These transducers come in various sizes and measurement modes, requiring only small amounts of reagents, bioreceptors, and analytes, making them ideal for medical diagnostics [3,4], biotechnology [5,6], and environmental monitoring applications [7,8] that require multispectral capabilities. Notable applications of these devices include plague control and environmental monitoring in agriculture to detect insecticides, fungicides, and herbicides, each related to controlling insects, fungi, and undesirable plants, respectively. These reagents are commonly referred to as pesticides, and those of chemical origin pose significant risks to human health and the environment [9].

Piezoresistive microcantilever biosensors have gained popularity in biosensing due to their high sensitivity and reliability. These sensors measure the surface stress-induced resistance change to study the analyte-receptor type bonding interactions, making them valuable in various medical and environmental applications. However, improving the sensitivity of these biosensors remains a challenge. In recent years, researchers have explored different approaches to improve the performance of piezoresistive microcantilever biosensors, including introducing stress concentration region (SCR) designs in the cantilever, as reported in Refs. [10-12].

In this context, piezoresistive microcantilevers experience numerous perturbations during immunological biodetection processes, which are normally conducted in an aqueous medium, increasing the likelihood of inducing spurious transduction signals. One of the primary challenges in developing devices based on piezoresistive microcantilevers as transduction elements for analyte biodetection is the immunoassay microfluidic cell. This cell is responsible for connecting the piezoresistive microcantilever chip to an electronic amplification module that acquires the transduction signal, subsequently analyzed to calculate the detected analyte concentration. The chip integrates contacts connecting to piezoresistors implanted on the microcantilevers in a Wheatstone bridge arrangement through prior microfabrication processes. In this circuit, the variable resistance is a piezoresistance implanted on the working microcantilever, and residual stresses caused by the interaction between the analyte and the bioreceptor immobilized on its surface, modify the re-

sistance's magnitude, resulting in variations in the circuit's measured voltage [13].

For correct operation, the microfluidic cell must also ensure that the necessary reagents in the immunological processes pass through the test chamber without spilling, as the reagents can generate recirculations or pressure changes that can affect the tightness or even the integrity of the cantilevers. In this sense, several papers report on the response of microcantilevers to fluid flow. For example, Nezhad *et al.* [14] proposed a method to fabricate PDMS microcantilevers intended for microsensors. They characterized detection limits through experiments and 3D fluid-structure simulations. Jana *et al.* [15] investigated the flow-induced mechanics of microcantilevers using semi-analytical methods and compared them with experimental observations. Their model was developed by conducting 3D fluid flow simulations to understand the flow behavior inside an empty cell, that is, without a microcantilever. The simulation results were then used to perform 2D steady-state simulations of the flow past the cantilever's tip, to compute the drag coefficients as functions of Reynolds number. Finally, using Euler-Bernoulli beam theory along with the calculated drag coefficients, the authors proposed an analytical equation to estimate the cantilever deflection as a function of the Reynolds number, which was validated using experimental observations. Lee *et al.* [16] characterized the flow and resistance change of an octagonal microcantilevers array designed for a flow-rate/flow-direction microsensor. Pressure distribution over each microcantilever was computed for different designs of the octagonal array to find the optimal configuration.

Of particular interest are those works analyzing non-conventional geometries for microcantilevers. For instance, Wu *et al.* [17] studied the flow-induced deflection and reactive rate as functions of the flow velocity for rectangular and triangular microcantilevers, suggesting the optimal placement of the cantilevers in the middle of the channel to minimize disturbances due to the flow field. For their part, Khanafer *et al.* [18] analyzed the effect of the magnitude and direction of the inlet velocity on the microcantilever deflection, using a finite element formulation based on a Galerkin method implemented in ADINA (v9.05, ADINA 182 R&D, Inc., Watertown, MA). In more recent studies, the authors have paid attention to designing, simulating, and optimizing the mechanical performance of truss-based microcantilevers [19,20]. This geometry minimizes the influence of the surrounding medium, thus resulting in increased sensitivity for water and ethanol as working fluids. However, it is worth noting that all of these papers focus on examining the microcantilever's response under a single configuration for fluid inlet/outlet, thus overlooking the potential impact of the microcell design on the fluid dynamics and, consequently, the sensitivity of the device.

Analyzing the behavior of microcantilever-based biosensors requires solving an FSI problem, which involves simultaneously addressing the fluid and structural equations to capture their interaction. Various numerical tools are available for solving such problems. For example, in Ref. [21], COMSOL Multiphysics was employed to study the flow around a flexible flap in a microchannel. Alternatively, open-source solvers for fluid flow and solid mechanics can be effectively coupled using the preCICE library. This library facilitates efficient data exchange, mapping, and synchronization between solvers, ensuring accurate and consistent coupling between software. Some implementations of FSI solutions for a flexible flap using open-source software can be found in Refs. [22,23].

This paper presents a 2D fluid-structure interaction study inside a microfluidic cell. The focus of the analysis lies in the description of the fluid dynamics and analyte concentration distribution around the cantilever beam for three different inlet/outlet configurations. This aspect should be an important factor when designing microfluidic cells for biological or pesticide detection. Since a desirable feature of these devices is to ensure that the sample comes into contact with the sensing surface, we performed an in-depth study of both, the mechanic behavior of the beam, as well as of the concentration of an analyte varing the inlet flow rate. This study will help to generate design guidelines for the flow configuration in the microfluidic cell, aiming to reduce the spurious measurement signals resulting from the interaction between the microcantilever and the working fluid.

The structure of the paper is as follows: In Sec. 2 the conceptual design of the microfluidic cell, as well as the KANAN.PESTI project are described. Section 3 describes the mathematical model, equations and boundary conditions used to simulate the system. In order to validate the numerical implementation, in Sec. 3.1 we present a comparison of the numerical model and previously reported experimental and theoretical analyses, finding good agreement. Results of the performed simulations are presented in Sec. 4, where the mechanical behavior of the beam, the fluid dynamics around the microcantilever and the spatial concentration field of the analyte are described in detail. Finally, the conclusions of the paper are presented.

2. Microfluidic cell design

This research is part of a larger project aimed at designing and manufacturing a biosensing platform named "KANAN.PESTI", which is intended for pesticide detection with high sensitivity, specificity, and portability. The project was funded by the Mexico's National Council for Humanities, Science, and Technology (CONAHCYT) through FORDECYT-PRONACES, currently program F003, with ID number 618306/2020.

In the following, a brief description of the general functioning of the biosensor is presented.

The design of the immunoassay cell considers the housing of a square-shaped chip measuring 9×9 mm^2 and 500 μm in thickness (refer to Fig. 1).

Inside the chip, there is a concentric 2×2 mm^2 square cavity containing two microcantilevers working as transduc-

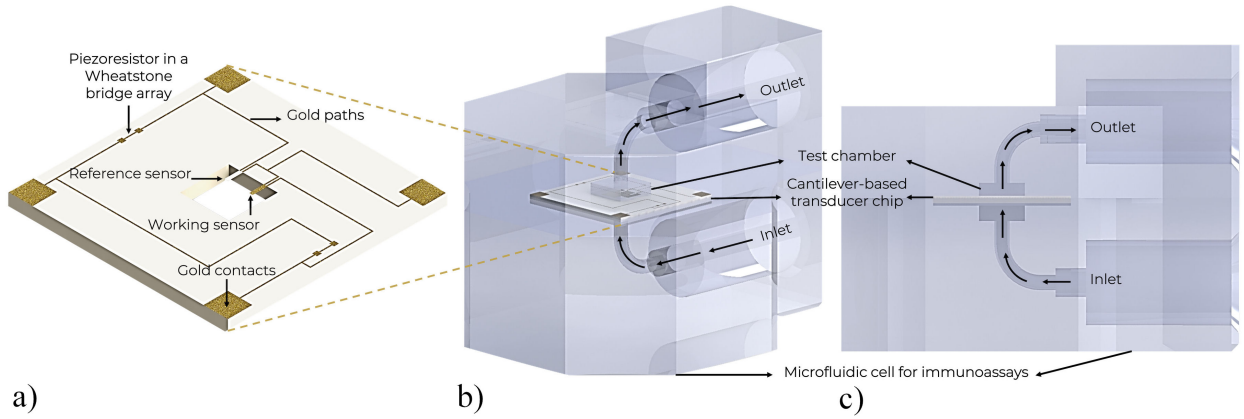

FIGURE 1. Sketch of the microfluidic cell for the KANAN.PESTI project.

ers. Each microcantilever is embedded with a piezoresistor, and both transducers are connected to external resistors, forming a Wheatstone bridge configuration. The corners of the chip have electric gold contacts that facilitate the connection of the Wheatstone bridge. One of the microcantilevers is functionalized and coated with bioreceptors on its surface, while the other serves as a reference transducer. Despite exposing both transducers to the analytes, only one detects their presence during an immunological reaction.

The microfluidic cell design serves two primary purposes. First, it ensures the tightness of the aqueous working medium (Sodium phosphate buffer PBS, pH 7.5) around the transducer. This tightness is achieved by incorporating concentric o-rings on the upper and lower surfaces of the cavity. When properly secured, these o-rings keep the PBS inside the immunoassay area. The microfluidic cell design considers strategically positioned microchannels as inlet and outlet channels for introducing and removing reagents during the immunological processes [refer to Figs. 1b)-c)]. The flow of PBS within the inner chamber remains constant.

Additionally, the immunoassay cell allows the connection between the chip and a signal acquisition module. It incorporates four retractable probes or pogo-pins that connect the chip and the electronic read-out module. These probes enable the analysis of the transducer's behavior during immunoassays. Therefore, the microfluidic cell design presents several challenges: 1) ensuring that the cantilevers are not damaged during reagent injection, 2) minimizing the vortices zones during the immunoassay within the chamber, 3) preventing the isolation of analytes on the transducer surface due to potential flow currents in the inner chamber, and 4) minimizing the effect of the inlet and outlet configuration on the deformation and mechanical stress in the cantilever. Those challenges can be addressed by a deep study of the fluid-structure interaction inside the microfluidic cell chamber and, therefore, choosing working flow conditions that allow them to be overcome.

2.1. Analyzed microfluidic cell configurations

Since this paper is intended to serve as a basis for the design of the microfluidic cell for the KANAN.PESTI biosensor, we propose and analyze three different inlet/outlet configurations to assess their effect on the deflection of the microcantilever and the flow dynamics. Those configurations were chosen since they represent design options for the microfluidic cell for the piezoresistive sensor. The results of the simulations will be quite relevant for the biosensor development process since accurate knowledge of the flow-induced deflections can help to improve its sensitivity by providing design and fabrication guidelines to minimize noise or spurious deformation due to fluid flow over the cantilever. Additionally, the flow dynamics prediction will be useful to improve the exposure of the biorceptors to the analytes, since it depends on how much of the injected contaminated fluid is directly in contact with the sensing surface. All the simulations were carried out in a 2D Cartesian domain, as shown in Fig. 2a). The corresponding dimensions of the domain, microcantilever, and inlet/outlet diameters are reported in Table I. It is important to highlight that all the dimensions were chosen considering the manufacturing capabilities of the microfabrication team in charge of developing the piezoresistive biosensor. Additionally, it has been defined that the biodetectors will be placed on the bottom surface of the microcantilever.

TABLE I. Microcell dimensions considered in the present study.

Fluid domain		Microcantilever		Inlet/Outlet	
Length, L	3 mm	Length, l	100 μm	Inlet diameter, l_{in}	1 mm
Height, H	2.5 mm	Height, b	1.15 μm	Outlet diameter, l_{out}	1 mm

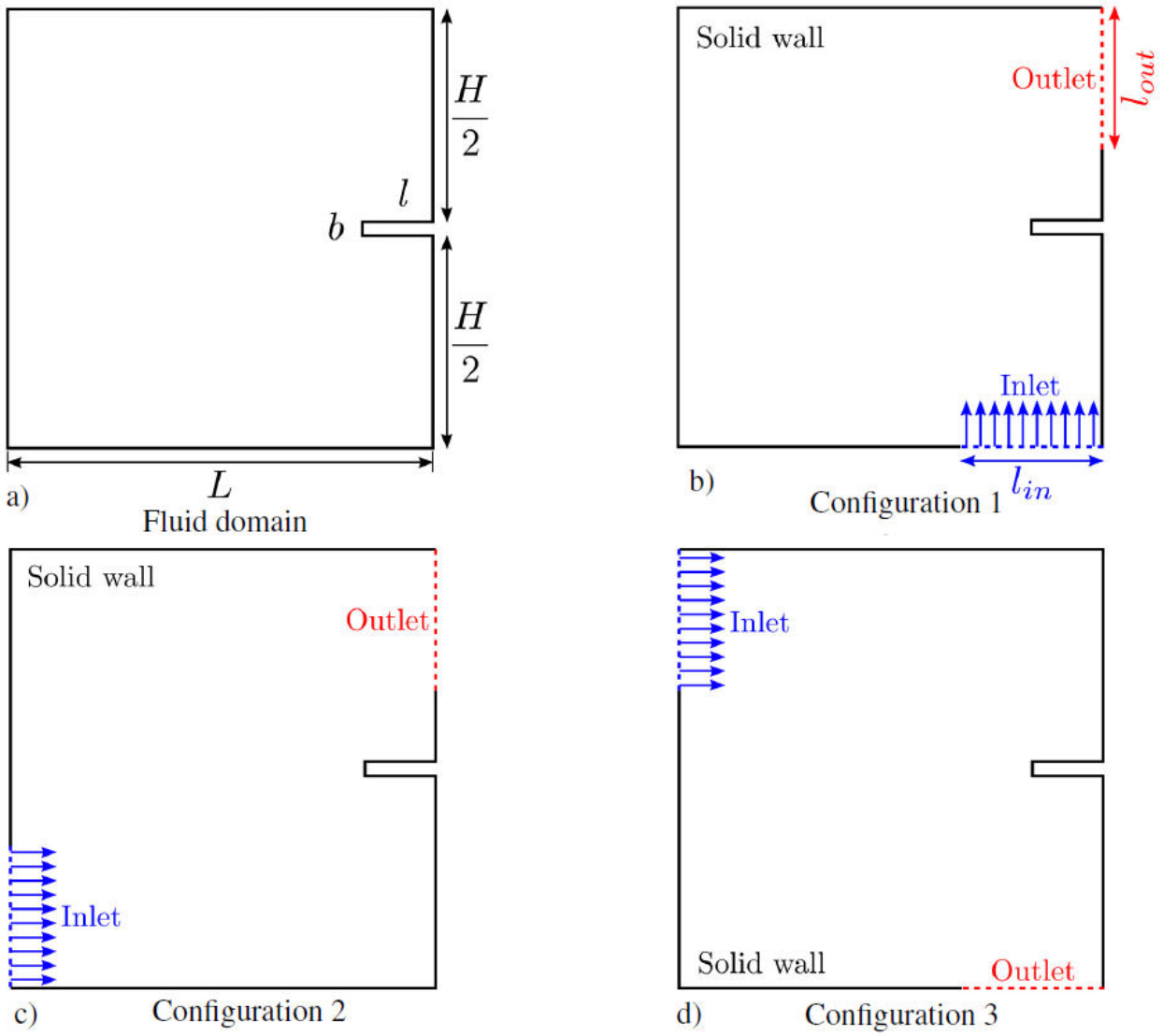

FIGURE 2. Sketch of the a) fluid domain and b)-d) different configurations used in the FSI simulations. The blue, red and black lines represent the inlet, outlet and solid walls in the domain, respectively.

Figure 2 shows the different configurations studied in the present paper. In Fig. 2a), the fluid domain is shown, whereas Figs. 2b)-2d) sketch the three analyzed cases. For all the cases, the inlet flow rate varied in the range from 20 to 4000 μl/min. The working fluid employed is common water, while the microcantilever is made of silicon, whose properties were taken from Table II (see Sec. 3.1). Although, the common fluid used in microsensors is a buffer PBS solution, it is normally so dilute that, from a fluid dynamics point of view, its important physical properties, *e.g.* mass density and viscosity, are those of water.

3. Mathematical model and numerical implementation

The microfluidic cell is studied by using a two-dimensional approach of a fluid-structure interaction model. Two-dimensional models have been widely used in investigating fluid-structure interaction within systems featuring microcantilevers [18,24-26]. The physical laws of interest for this paper consist of mass conservation and balance of momentum for the fluid, which, for an incompressible and Newtonian fluid, can be expressed as

$$\nabla \cdot \mathbf{v} = 0, \tag{1}$$

$$\frac{\partial \mathbf{v}}{\partial t} + (\mathbf{v} \cdot \nabla)\,\mathbf{v} = \frac{1}{\rho}\nabla \cdot \left[-p\mathbf{I} + \mu(\nabla \mathbf{v} + \nabla^T \mathbf{v})\right], \tag{2}$$

where $\mathbf{v}$ and p are the velocity and pressure fields, and ρ and μ are the mass density and dynamic viscosity of the fluid, respectively. $\mathbf{I}$ is the second-order unit tensor. For all the reported simulations in this paper, the material properties for both, the solid and fluid phases were considered constant. Considering these physical properties, the corresponding Reynolds number is given by

$$Re = \frac{v_0 l}{\nu}, \tag{3}$$

v_0 being the inlet flow velocity corresponding to the given flow rate, l the length of the cantilever and ν the kinematic viscosity of the fluid. As a result, the range of Reynolds number analyzed corresponds to $0.04 \leq Re \leq 8.4$, corresponding to laminar flow.

Since we are interested in the fluid-structure interaction (FSI), the surface of the microcantilever in contact with the fluid is considered as a common interface. In this surface, the microcantilever experiences a force due to the fluid motion given by

$$\mathbf{F} = -\mathbf{n} \cdot \left[-p\mathbf{I} + \mu(\nabla \mathbf{v} + \nabla^T \mathbf{v})\right], \tag{4}$$

where $\mathbf{n}$ is the unit vector normal to the cantilever's surface. At the same time, the fluid attaches to this interface, thus acquiring the same velocity as the microcantilever. Standard no-slip boundary conditions were applied to all solid surfaces.

The mechanical behavior of the cantilever can be computed by the Navier-Cauchy equation:

$$\frac{d^2\mathbf{u}}{dt^2} = \nabla \cdot \boldsymbol{\sigma} + \mathbf{F}, \tag{5}$$

where $\mathbf{u}$ is the displacement vector and $\boldsymbol{\sigma}$ is the stress tensor that is calculated by using the generalized Hooke's law for an isotropic material.

Figure 3 shows a sketch of the considered domain of interest. For the fluid domain, standard no-slip boundary conditions were applied at all solid surfaces (green solid lines), whereas, a constant flow rate was prescribed perpendicular to the inlet of the flow domain (dashed blue line). A prescribed constant zero pressure is imposed at the outlet of the domain (dashed black line), which physically implies a fully-developed flow. In mathematical terms:

$$\text{Interface: } \mathbf{v} = \mathbf{v}_m, \quad \text{Solid walls: } \mathbf{v} = 0, \tag{6}$$

$$\text{Inlet: } \mathbf{v} = \mathbf{v}_0, \quad \text{Outlet: } \frac{\partial \mathbf{v}}{\partial n} = 0, \tag{7}$$

where $\mathbf{v}_m$ and $\mathbf{v}_0$ are the microcantilever's interfacial velocity and inlet velocity of the fluid, respectively. $\mathbf{v}_0$ was calculated considering the working inlet flow rates, that is, by diving the flow rate by the inlet surface area.

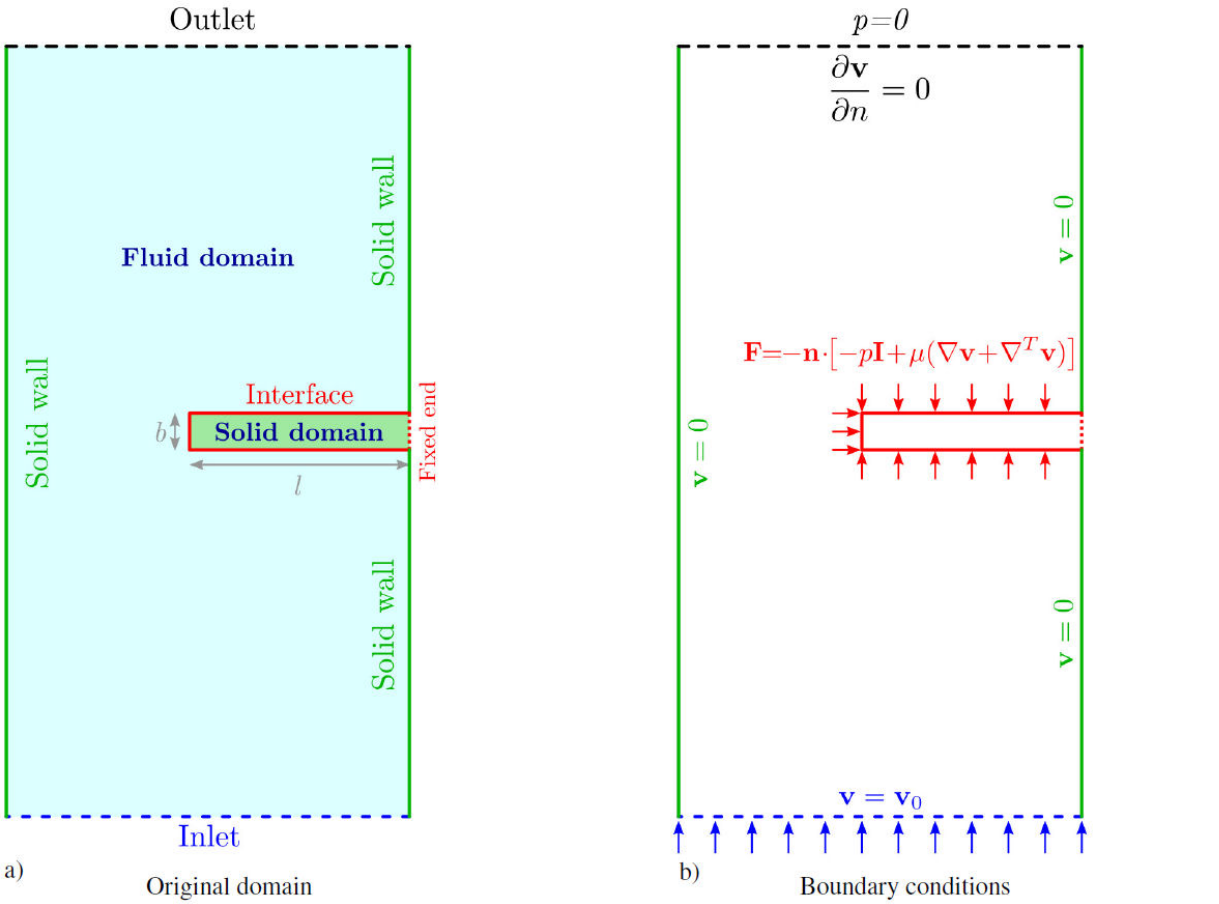

FIGURE 3. Sketch of the coupled system fluid-structure considered for the microfluidic cell. a) Domain of interest and b) Boundary conditions. The important dimensions for the cantilever are its thickness, b, and length, l.

The microcantilever's surface in contact with the fluid (solid red line) is subjected to the load exerted by the flow, as described by Eq. (4), and its rightmost side (dashed red line) is kept fixed at its initial position.

System (1)-(5), with the corresponding boundary conditions, Eqs. (6) and (7), was numerically solved using the preCICE coupling library [27]. The fluid equations were solved using the Open-source Field Operation And Manipulation (OpenFOAM) v1806 library [28,29], whereas the solid mechanics model was solved using the deal.II FEM open-source software [30,31]. Since the microcantilever is expected to deform considerably, a moving mesh algorithm must be considered for the fluid domain. For all the reported simulations in this paper, the *pimpleFoam* solver, which has dynamic mesh generation capabilities, was used. This solver combines the SIMPLE (Semi-Implicit Method for Pressure-Linked Equations) and PISO (Pressure-Implicit with Splitting of Operators) algorithms. The algorithm iteratively solves Eqs. (1) and (2) by alternating between velocity and pressure corrections, using outer SIMPLE algorithm loops for steady-state convergence and inner PISO algorithm loops for time-dependent adjustments. The convective terms of the Navier-Stokes equations were discretized using a second-order upwind limited scheme and the diffusive terms with a central differences scheme. The resulting linear systems were solved with a Conjugate Gradient method combined with a Diagonal-based Incomplete Cholesky preconditioner.

Due to the simple geometry of the fluid domain, the initial 2D mesh generated consists of quadrilateral cells. Since the zone around the microcantilever is the most important region for this study, the meshing strategy included a refinement of the mesh as we approach the cantilever's tip from any of the two spatial directions. Considering that the thickness b is the most critical physical distance and that the largest deflections will be present in this region, the mesh was created so that the cells near the tip of the cantilever are squares, that is, their aspect ratio is close to unity. Figure 4a) shows an example of the initial mesh used in this study, whereas Fig. 4b) depicts a dynamic mesh adjusted to account for the microcantilever's deflection. The blue lines correspond to the mesh generated for the fluid, while, for the solid domain, we used a uniform mesh consisting of square cells, shown in red in the zoomed region of Figs. 4a) and 4b).

As can be seen in Fig. 4, the meshes for the solid and fluid regions of the system are non-conforming, namely, they do not perfectly align at the interface. The information exchange between the two employed software packages (OpenFOAM and deal.II FEM) is handled by the preCICE coupling library through a radial basis function (rbf).

Finally, in order to analyze phenomena more related to real situations, we also performed simulations of the behavior of a passive scalar inside the microcell. This phenomenon is governed by the advection-diffusion equation:

$$\frac{\partial C}{\partial t} + (\mathbf{v} \cdot \nabla)\, C = D_m \nabla^2 C, \tag{8}$$

where C and D_m are the concentration and mass diffusivity of the analyte, respectively. For all the reported results, we considered a diffusivity of 1.39×10^{-9} m^2/s, which corresponds to the diffusion coefficient of urine in water. This was chosen this way because one of the working fluids to use in the biosensor corresponds to the urine of the population. To mimic the operation process of the microcell, we started the simulations by injecting a fluid with no analyte concentration. When the steady state has been reached, a sample of 50 μl, with initial concentration $C_0 = 50$ μg/ml, is injected into the cell at the same flow rate. When this sample has been depleted, then the inlet concentration is switched back to zero. As the sample flows through the cell, the concentration of the analyte at the lower surface of the cantilever was monitored through the simulations. Since no sensing kinetics is implemented in the present study, in all solid boundaries,

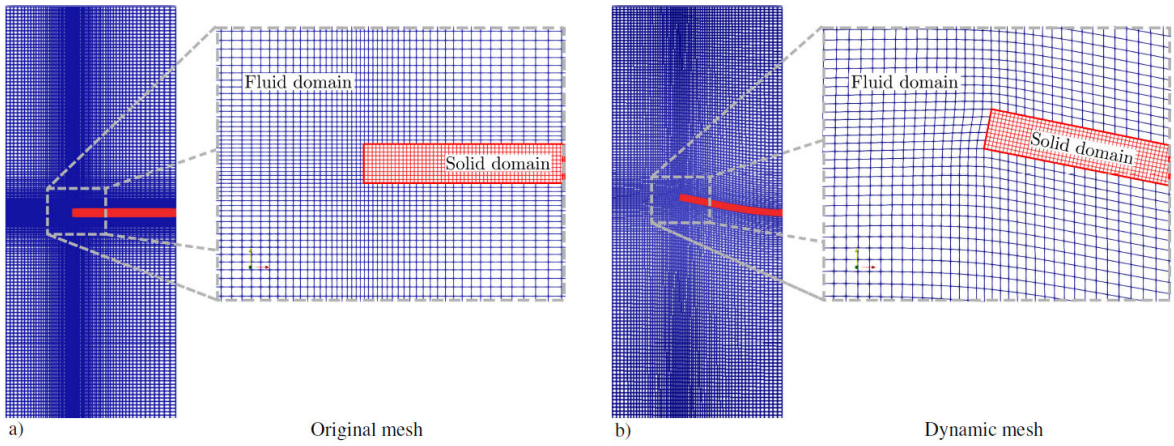

FIGURE 4. a) Example of a refined mesh near the microcantilever. The zoomed region shows that, in the fluid domain, the mesh is finer near the tip of the microcantilever, and gets coarser as we move away from this region. For the solid domain, the mesh consists of uniform square cells for the whole cantilever. b) Example of an adjusted mesh as the solid deforms.

TABLE II. Material properties and physical parameters used for validation.

Solid properties		
Parameter	Nezhad *et al.* [14]	Jana *et al.* [15]
Material	PDMS	Silicon
Young modulus, E	802 kPa	169 GPa
Poisson's ratio, ν_r	0.45	0.28
Density, ρ_s	970 kg/m^3	2330 kg/m^3
Microcantilever's thickness	40 μm	1 μm
Microcantilever's length	510 μm	500 μm
Fluid properties		
Parameter	Nezhad *et al.* [14]	Jana *et al.* [15]
Working fluid	Water	Liquid Nitrogen
Fluid density, ρ	1000 kg/m^3	1.616 kg/m^3
Fluid viscosity, $\nu = \mu/\rho$	1×10^{-6} m^2/s	1.081×10^{-5} m^2/s
Flow rate range	$0.2 - 1$ ml/min	$20 - 60$ ml/min

including the microcantilever, Neumann conditions were implemented, that is, the first derivative of the concentration field is equal to zero, whereas at the outlet of the domain, fully developed behavior is enforced. The solution of this phenomenon was also performed using OpenFOAM [29].

3.1. Validation

In order to validate the numerical implementation, simulations for two microcantilever-based flow sensors reported in the literature were performed. On the one hand, the experimental measurements made by Nezhad *et al.* [14] were reproduced by our simulations. The system consists of a PDMS cantilever in a microfluidic cell in which the flow is perpendicular to the length of the cantilever. For this first validation, we used the exact geometry and flow rate ranges as reported by the authors [14]. On the other hand, simulations were also performed for the experimental system reported by Jana *et al.* [15], which is conformed by a silicon microcantilever immersed in a flow. For both cases, simulations were carried out for the different flow rates reported in the respective references.

Table II shows the considered theoretical and experimental parameters, as well as material properties, used to validate the numerical simulations. All these values were taken from the corresponding references.

As can be seen from Table I, the selected cases for validation have very different physical parameters, particularly, the flow rate ranges, material properties, and cantilever's thickness, which results in deflections with three orders of magnitude differences. Nevertheless, the implemented 2D numerical model was able to reproduce the same behavior reported by Nezhad *et al.* [14] and Jana *et al.* [15], thus validating the numerical model.

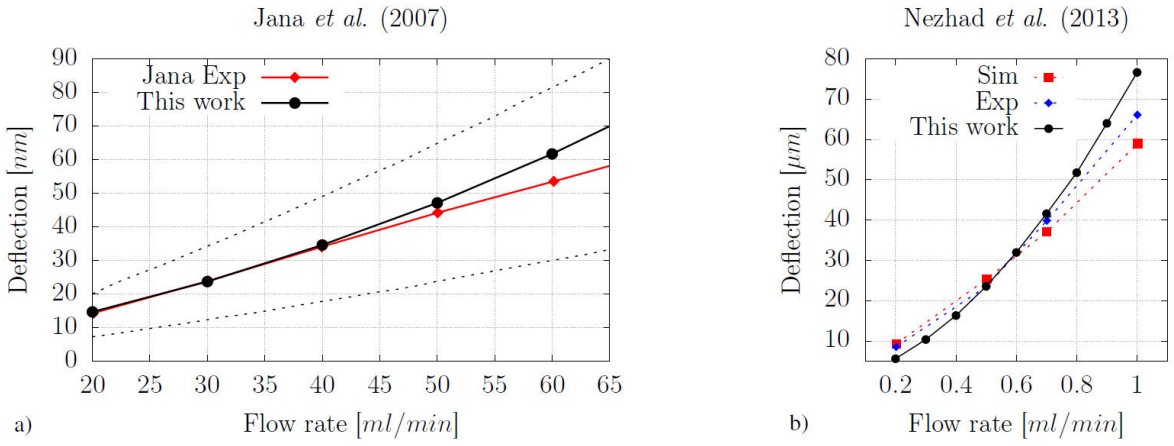

FIGURE 5. Validation of the implemented 2D numerical model. Experimental microcantilever deflections (solid red and dashed blue lines) reported by a) Jana *et al.* [15] and by b) Nezhad *et al.* [14] are in good agreement with the simulated results (solid black line) of the present paper. In a), black dashed lines mark the lower and upper limits of Jana's semianalytical model [15].

In Fig. 5, the deflection of the cantilever's tip is plotted as a function of the flow rate for the two selected parameter sets: $a)$ silicon cantilever [15], and $b)$ PDMS cantilever [14]. As it can be observed, the results of the simulations for both systems are in good agreement with the reported experimental measurements. It is important to highlight that in the case of the silicon cantilever [Fig. 5a)], the numerical results begin to deviate slightly from the experimental measurements when the flow rate is larger than 40 ml/min, this can be explained by two main reasons: 1) at those high velocity flows, three-dimensional effects can be important and change the force distribution over the cantilever, and 2) the flow produces large equivalent stress that promotes a nonlinear behavior of the silicon cantilever, and then, the elastic model is clearly not valid. However, the flow rates at which the Biosensor designed in the present project will work, are much lower than this limit ($<$1 ml/min), and then the validity of the two-dimensional approach can be safely used. It is worth mentioning that the black dashed lines in this figure represent the lower and upper limits of Jana's semianalytical model developed in their study. Particularly, these limits mark the extreme values of geometry dimensions (length and thickness) of their corresponding analytical adjustments. In this study, we only performed simulations with the same cantilever geometry as the one they reported experimentally, thus only the red line is used for comparison.

In Fig. 5b), a comparison of our numerical implementation with the results reported by Nezhad [14] is presented. It can be noted that this implementation presents a good agreement with the results previously reported, even though our model deviates slightly from both the experimental and simulated results by Nezhad. In this sense, it is noteworthy that this second case was used only to validate our FSI implementation, considering very different physical properties and geometry than the actual biosensor that will be fabricated. The main objective of the KANAN.PESTI project involves the development of a biosensor made of silicon, operating at flow rates in the order of μl/min, conditions for which our model is accurate and reliable, as seen in Fig. 5a).

4. Results

4.1. Fluid flow behavior

In the same way as in the validation stage, the governing equations Eqs. (1)-(5) and boundary conditions Eqs. (6) and (7) were solved for the three selected domains varying the inlet flow rate. Also, the same numerical implementation was followed, that is, a mesh refinement around the microcantilever's tip in the fluid domain and a uniform meshing for the solid; dynamic meshing to account for the deflection of the cantilever, and the coupling of OpenFOAM [28,29] and

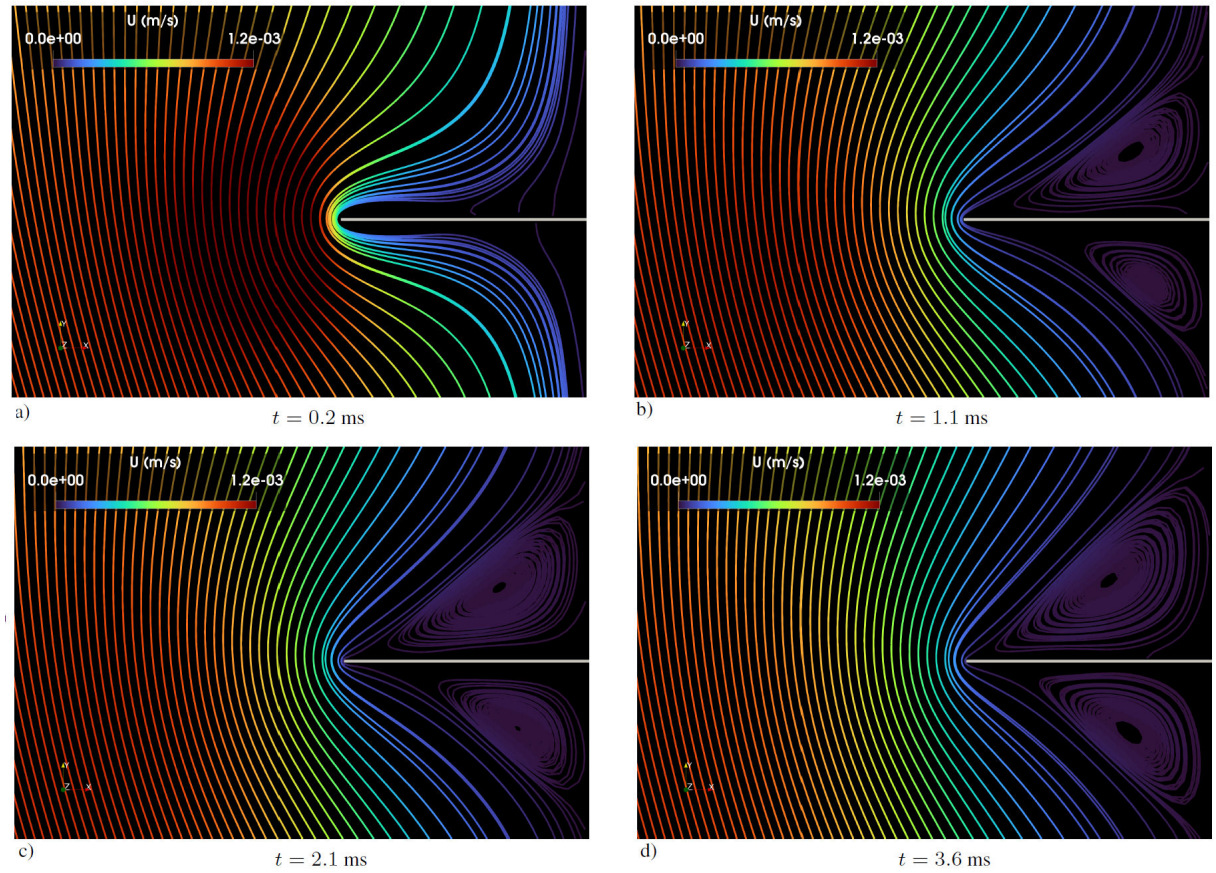

FIGURE 6. Time evolution of instantaneous flow streamlines for an inlet flow of 100 μl/min in Configuration 2.

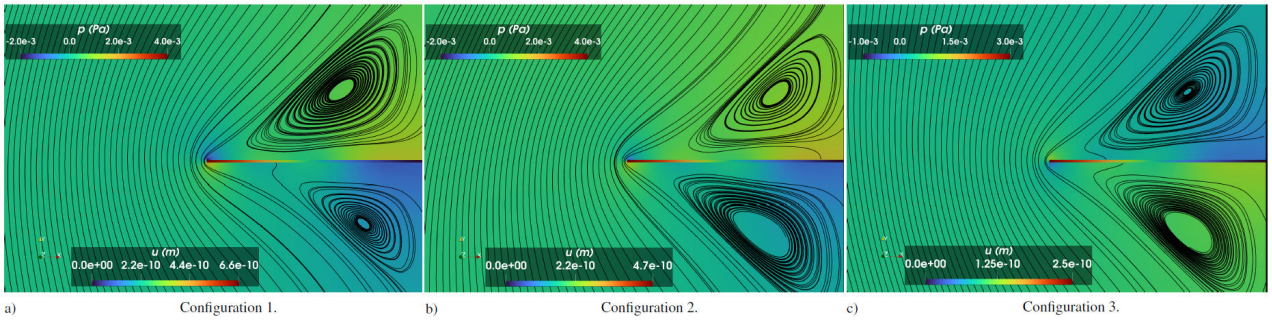

FIGURE 7. Streamlines for a 750 μl/min inlet flow for the three configurations in steady state.

and deal.II [30.31] software through the preCICE coupling library [27].

Figure 6 shows the time evolution of the flow around the microcantilever for a 100 μl/min inlet flow rate in configuration 2. In all images, instantaneous streamlines are used to illustrate the fluid motion. Just at the beginning of the simulation [$t = 0.2$ ms, Fig. 6a)], the flow is very symmetrical around the cantilever. As time passes, for $t = 1.1$ ms, [Fig. 6b)], two vortices are formed, thus breaking the original symmetry of the streamlines. Next, for longer times [$t = 2.1$ ms, Fig. 6c)] the vortices become larger until they reach an almost steady state for $t = 3.6$ ms [Fig. 6d)]. This behavior is similar for small flow rates ($<$1000 μl/min).

Even though there are small differences in the flow inside the analyzed configurations, for small flow rates the qualitative behavior of the dynamics is the same, that is, symmetry around the solid beam for short times, followed by the formation of two vortices wrapping around the microcantilever, and breaking of the symmetry, which is maintained even when reaching steady state. However, as the inlet flow rate increases, configuration 3 seems to present less asymmetry when compared to the other two configurations. Figure 7 shows the flow streamlines and pressure field for the three configurations, for an inlet flow of 750 μl/min in a steady state. As it can be observed, configuration 3 shows a more symmetric flow pattern than the other two configurations. This can be explained since the outlet of the flow region is located far from the cantilever, thus providing a large developing length, which allows a more symmetric pressure distribution on the cantilever's surface. As a result, smaller flow-induced deflections are observed for this configuration. From the pressure field, it can be observed, for all configurations, that the maximum pressure is located at the tip and fixed end of the cantilever, in opposite locations of the longitudinal cantilever surfaces. The same happens with the minimum values for the pressure. Finally, the highest pressures are found in Configuration 1, indicating that the largest deflections will be found in this configuration. This is confirmed by analyzing the displacement of the cantilevers (u) for the three configurations shown with the contour field inside the solid domain (cantilever beam). The largest deflection is observed in Configuration 1, caused by the flow generated in this configuration. Furthermore, it can be noted that, for all three cases, the deflection remains below 1 nm under these flow conditions.

Despite the symmetry of the flow around the cantilever beam is a desirable feature, since it diminishes flow-induced noise, it can have an adverse effect. For instance, in real operation conditions, after steady state has been reached, an inlet flow enters the microfluidic cell with an initial concentration of the analyte of interest, which is expected to be deposited on the cantilever's surface, however, the existence of the two vortices may act as a flow barrier that prevents the incoming flow to be in direct contact with the detecting surface. As a result, when the analyte concentration of the recirculating fluid is depleted because of deposition, the incoming, high-concentration fluid will pass far from the cantilever, meaning that the analyte will travel toward the detecting surface mainly by diffusion. This particular situation may have an important impact on the performance of the detection system, since the diffusion mechanism might not be quick enough to allow a correct detection. Then, there must exist a well-compromise between the flow-induced noise that deflects the cantilever and the flow developed in the cell to ensure adequate detection.

Since the biodetectors will be placed on the bottom surface of the microcantilever, it is convenient to minimize flow recirculations at this region in order to improve the transport of the analyte, via a combined convection-diffusion mechanism. This feature intrinsically will improve the sensitivity of the biosensor, and, at the same time, decrease the time required for detection, since the analyte sample can quickly pass around the bottom surface of the microcantilever and interact with the detectors. For this purpose, simulations at larger flow rates were implemented in order to find the most suitable flow and inlet/outlet configuration, with the objective of minimizing both, the flow recirculations close to the detection zone, and the cantilever deflection in such a way that the detection sensitivity of the biosensor is not compromised. Figure 8 shows the temporal evolution of the flow inside the cell for a flow rate of 2000 μl/min in Configuration 1. As can be noticed, after the symmetry is broken only one vortex above the microcantilever appears for these flow conditions. This recirculation grows as a function of time until the flow reaches a steady state.

Similarly, as for small flow rates, it is possible to compare the qualitative steady flow for the three different inlet/outlet

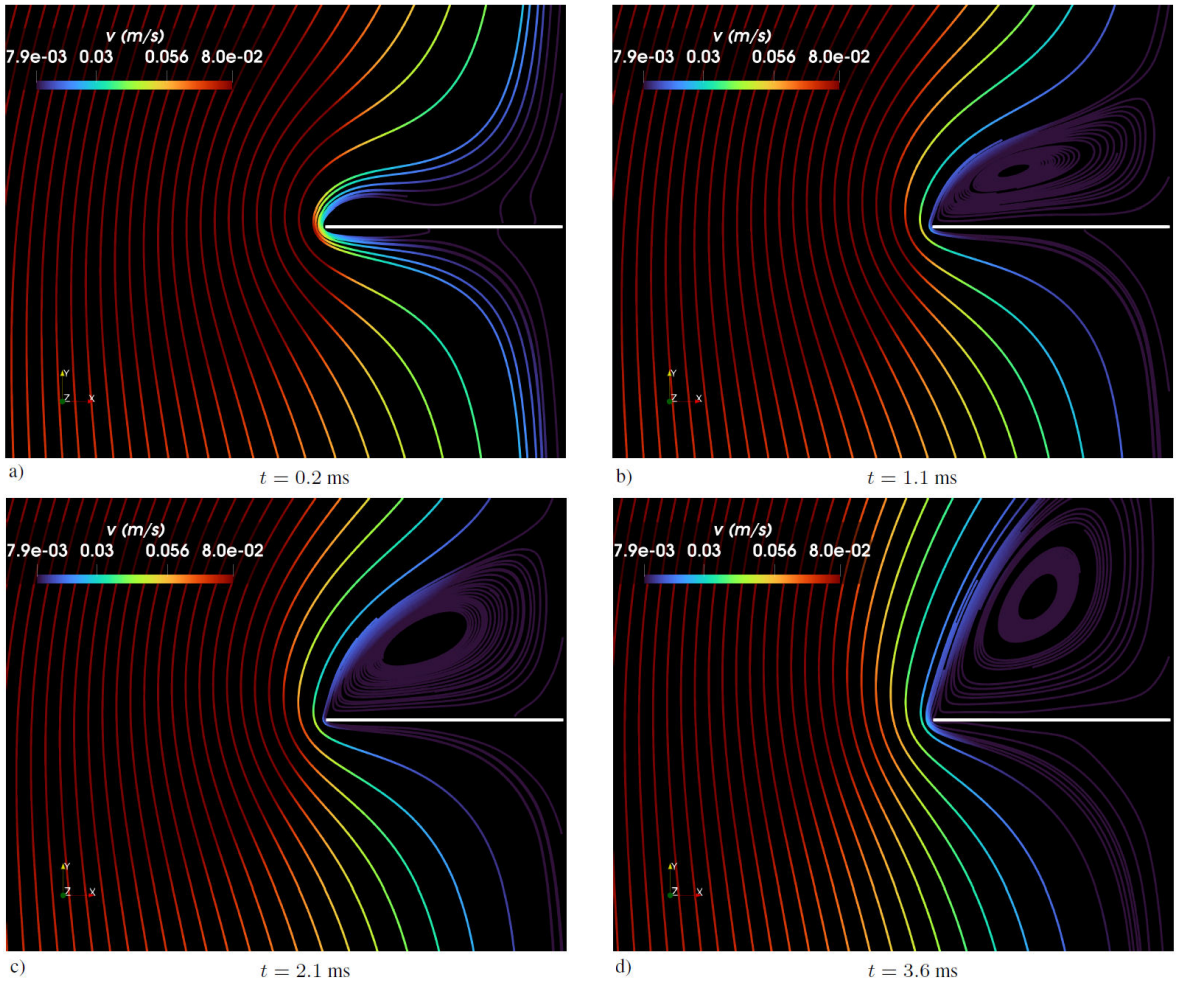

FIGURE 8. Time evolution of the instantaneous flow streamlines for an inlet flow of 2000 μl/min in Configuration 1.

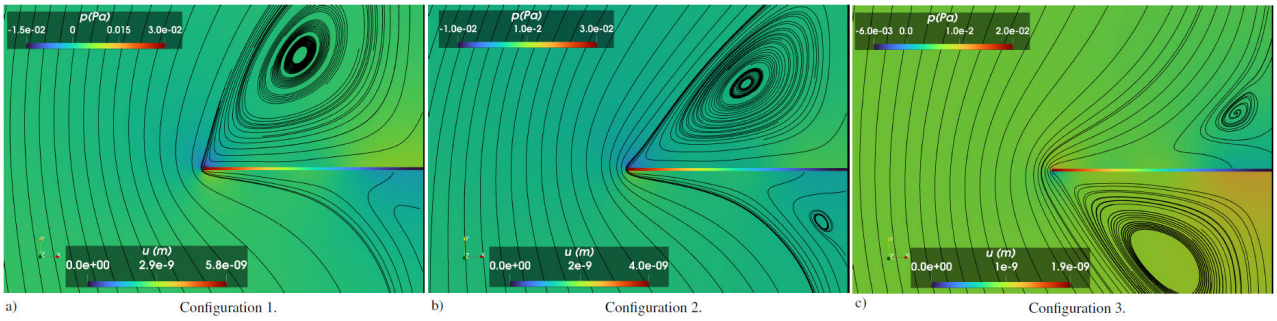

FIGURE 9. Streamlines for a 4000 μl/min inlet flow for the three configurations in steady state.

configurations. In Fig. 9, instantaneous streamlines and the pressure field are plotted for the steady flow for the three configurations and a flow rate of 4000 μl/min. As it can be seen, when the flow rate is increased, the effect of the inlet/outlet configurations on the qualitative behavior of the flow is much more significant. In Configurations 1 and 2, the size of the vortex below the microcantilever is reduced at this flow rate, particularly, for Configuration 1, the vortex is constrained to the fixed edge of the cantilever [Fig. 9a)], this is convenient from the detection point of view since the detectors can be placed along almost the entire bottom surface of the beam. Configuration 2 can also be used at these higher flow rates, paying attention that the detectors must be placed beyond the middle of the microcantilever with respect to its root [Fig. 9b)]. Finally, Configuration 3 should be avoided if large flows are required (>2000 μl/min) since the vortex below the microcantilever grows as the flow rate increases [Fig. 9c)]. From the pressure field, it can be noticed a more

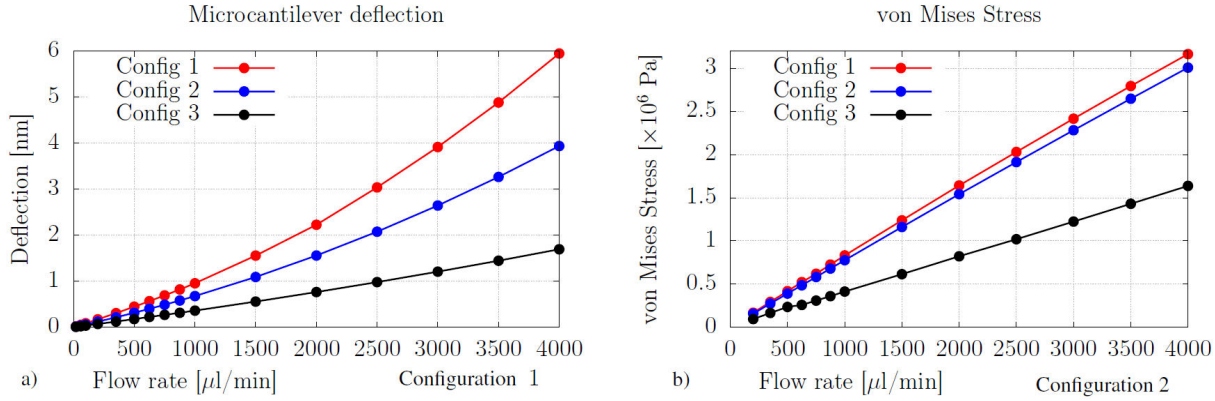

FIGURE 10. Comparison of a) the deflection and b) von Mises stress as functions of flow rate for the three considered configurations.

asymmetrical distribution than that for the 750 μl/min (see Fig. 7), hence the asymmetry of the flow.

4.2. Microcantilever mechanics behavior

Alongside the fluid mechanics, the quantitative behavior of the microcantilever mechanics was assessed for all the simulated conditions. Figure 10 shows the deflection of the microcantilever and maximum equivalent von Mises stress, as functions of flow rate, for the three considered configurations. It can be noticed that the microcantilever suffers the largest deflections using Configuration 1. The expected deflection during the real detection is around 50 nm, and the maximum deflection simulated for Configuration 1 is 5.8 nm, which represents more than 10% of the expected deformation during the operation of the biosensor. This can represent a risk from a sensitivity point of view, since flow-induced deformation is a source of noise for the detection process. On the other hand, with Configuration 3, the smallest deflections were found, however, as was commented in the previous section, this configuration has the problem that the vortex below the cantilever becomes larger as a function of the flow rate, and this is not convenient from the analytes transport point of view. Finally, for Configuration 2, the maximum deflection obtained is 4 nm, which is small enough not to compromise the detection sensitivity of the biosensor ($<$ 10% of the expected deflection due to the analyte detection).

Figure 10b) shows the maximum equivalent (von Mises) stress as a function of the inlet flow rate for the three configurations. As it can be seen, Configurations 1 and 2 exhibit very similar equivalent stresses, both of which have a linear behavior. On the other hand, Configuration 3 presents a much smaller von Mises stress, being less than 50% of the stress for Configuration 1 when the flow rate is 4000 μl/min. It is important that the exhibited stresses in all configurations are much smaller than the yield strength of the silicon, in order to ensure that the microcantilever will be working in the elastic zone of the material.

4.3. Analyte concentration analysis

To complete the study, we present the behavior of the passive scalar inside the microfluidic cell. Recall that this concentration fields were obtained by solving Eq. (8) after letting the system reach steady state, and then injecting a 50 μl sample with an analyte concentration of 50 μg/ml at the same flow rate. Figure 11 illustrates the spatial distribution of the analyte concentration for an inlet flow rate of 750 μl/min for the three configurations. For Configuration 1 [Fig. 11a)], since the analyte sample flows perpendicular to the lower surface of the cantilever, the concentration is higher in this region. It is worth noting that the concentration in this surface reaches higher values at approximately the first third of the microcantilever length, measured from its tip. This can be explained by the fact that, near the walls of the microcell, the fluid has

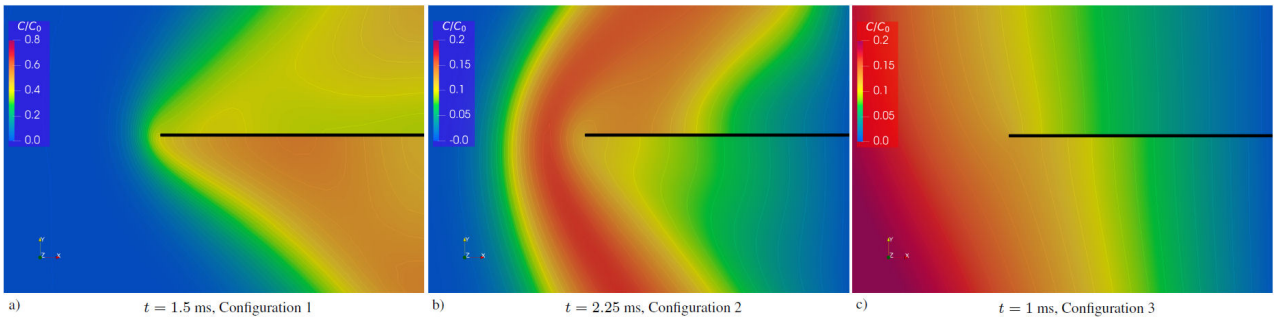

FIGURE 11. Spatial distribution of the analyte concentration for 750 μl/min for a) Configuration 1, b) Configuration 2 and c) Configuration 3.

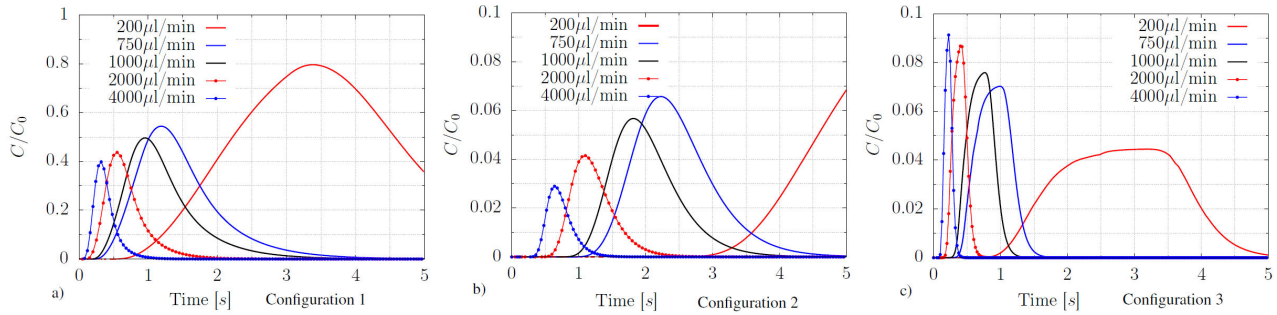

FIGURE 12. Concentration as a function of time for different inlet flow rates for the three analyzed configurations.

a very low velocity. Consequently, in this region, the transport of the analyte is dominated by diffusion, unlike the region away from the solid walls, where advection promotes transport of the analyte towards the cantilever's surface. This information can be valuable for the design and fabrication of such devices. For example, as a recommendation, the biological immobilization and functionalization of the cantilever's surface can be confined to the first half of the entire surface, ensuring sensitivity without compromising the device's performance.

For the other two configurations, an interesting situation occurs: by closely observing the spatial distribution of the analyte, it can be observed that the highest concentrations are found in the surface of the cantilever opposite to that of the inlet flow, that is, for Configuration 2 [Fig. 11b)] the inlet is located below the position of the microcantilever, whereas the outlet of the cell is in a higher position. The combination of this configuration, alongside the fact that the inlet is farther away from the cantilever beam than in Configuration 1, drives the fluid flow from the bottom up. Consequently, the fluid flow tends to transport the analyte away from the lower surface of the cantilever, and the mechanism responsible to transport the analyte to this surface is diffusion, whereas in the upper surface the combination of the two mechanisms (advection + diffusion) results in higher concentrations. For Configuration 3 [Fig. 11c)], the latter situation repeats itself but with the flow direction inverted, that is, the flow is driven from top to bottom, so that the higher concentrations are found on the lower surface of the microcantilever.

Figure 12a) displays the concentration (averaged over the lower surface of the cantilever) as a function of time, for different inlet flow rates in Configuration 1. As it can be seen, for lower flow rates, the concentrations near the cantilever are higher, reaching a maximum value of 80% of the initial inlet concentration for a flow rate of 200 μl/min. It can also be observed that the maximum concentration is achieved for smaller times as the inlet flow rates are larger. This is explained since the time required to inject the 50 μl of the sample is smaller for higher flow rates, thus diminishing the residence time of the analyte and, consequently, the available mass to be detected.

Figure 12b) shows the behavior of the mean concentration of the analyte as a function of time for Configuration 2. As it can be seen, this configuration presents the same behavior as Configuration 1 with two differences: first, the maximum concentration achieved in this configuration is one order of magnitude smaller than that for configuration 1; second, the time interval needed to reach this concentration is larger for all inlet flows. Considering that the diffusivity is the same for all simulations, these differences result from purely advective transport. As it can be observed in Fig. 9, even though the structure of the flow is similar, the larger velocities present in Configuration 1 promote higher advective transport, thus resulting in higher concentrations. Additionally, given the dimensions of the analyzed domain, it is worth mentioning that, for configurations 2 and 3, the inlet is located farther from the cantilever than it is for configuration 1. As a result, it is expected that the sample will diffuse to a larger region before approaching the space near the microcantilever, thus resulting in an overall decrease of the concentration near the sensing surface, which is evident from Fig. 12.

Figure 12c) displays the concentration profiles for Configuration 3. It can be easily noted that the order of magnitude for the concentration is similar to that of Configuration 2, but the behavior of the profiles is reversed compared to the previous configurations, that is, higher concentrations are achieved for higher flow rates. Another difference lies in the fact that the profiles flatten when maximum concentration is about to be achieved, which is more clearly seen for an inlet flow rate of 200 μl/min.

Even though the concentration of the analyte provides valuable information about the location of the functionalized surface, from a sensing perspective in these kinds of devices, the total mass reaching the sensing surface is of major importance, since is this quantity the one mainly responsible for deflecting the cantilever. In this sense, we calculated the available mass reaching the lower surface of the beam by means of

$$m_T = \int_0^t C(t) Q_0 dt, \tag{9}$$

where Q_0 is the inlet flow rate and $C(t)$ is the concentration profile at the sensing surface as shown in Fig. 11. The analyte concentrations for configuration 1 are, in general, much higher than for the other two configurations, as it can be seen in Figs. 11 and 12. Even though Fig. 11 is presented for par-

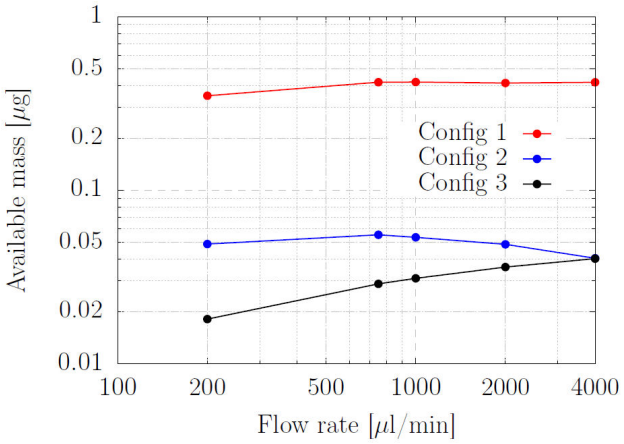

FIGURE 13. Total available mass at the cantilever's lower surface as a function of inlet flow rate.

ticular time instants, it is expected that the integral over time of this field presents this same behavior. Figure 13 displays the total mass reaching the cantilever as a function of the inlet flow rate for the three configurations. In Configuration 1 (red line) it can be seen that the total available mass is almost constant for all the analyzed flow rates. The reason behind the smaller mass for 200 μl/min lies in the fact that the time integration was performed for the first five seconds, which, for this low flow rate, is not enough for the analyte concentration to reach a value close to zero near the cantilever, as it can be observed in Fig. 12a) (red solid line). For Configurations 2 and 3 (blue and black lines in Fig. 13), the total available mass is one order of magnitude smaller than that of Configuration 1. For Configuration 2, it can be noted that the available mass reaches a maximum value at 750 μl/min and then decreases. For the final configuration, the total mass and the inlet flow rate are proportional.

5. Conclusions

In this paper, the interaction of a microcantilever with a fluid flow inside a microcell was investigated through 2D numerical simulations implemented using Open-Source software. The numerical model was validated using experimental and numerical results previously reported. The good agreement of the model with the validation data shows that Open-Source software, particularly, OpenFOAM, deal.II and the preCICE coupling library is a reliable implementation to perform accurate simulations of multiphysics phenomena of interest in biosensors and MicroElectroMechanical devices (MEMS).

The numerical results allowed us to describe the dynamics of the flow around the microcantilever, and the distribution of a passive scalar using different inlet/outlet configurations. For all the analyzed configurations at small flow rates, at the beginning of the simulations, the flow around the cantilever beam is symmetric, as time passes and the microcantilever deflects, two small vortices enclose the cantilever, thus breaking the symmetry. For longer times, the vortices become larger until reaching an almost steady state, that is, a state in which the deflection of the beam oscillates with small amplitude around a very small mean value. By varying the inlet flow rate, it was found that for flow rates below 1000 μl/min, the inlet/outlet configuration has no significant effect on the flow behavior, and the two vortices surrounding the microcantilever may act as a barrier that prevents the arrival of analytes to the cantilever's surface, thus, hindering and delaying the detection. For larger flow rates, the inlet/outlet arrangement has an important effect on the microcantilever deflection and the transport of the flow for ensuring that the analyte sample interacts efficiently with the detectors. It can be concluded that Configurations 1 and 2 are suitable for being used at flow rates less than 3500 μl/min. Above this flow rate, Configuration 1 can be used carefully since the deflection due to the cantilever interaction with the flow is more than 10% of the expected deflection by the detection process, which can compromise the sensitivity of the biosensor. In this sense, Configuration 2 shows a good compromise between the flow-induced deflection and the flow distribution for efficient biosensor detection. In this sense, it is shown that the FSI simulations should be focused on both, diminishing flow-induced noise, and, at the same time, fomenting favorable flow patterns to ensure proximity to the cantilever's surface of the inlet flow to be analyzed. From the analysis of the distribution of a passive scalar, it was also found that the inlet/outlet configuration influences the available amount of analyte reaching the detecting surface. For configuration 1 the analyte concentration is one order of magnitude higher than for configurations 2 and 3. This implies that the amount of analyte mass available in the cantilever area where the sensor detectors are located is significantly larger and reaches around 80% of the initial inlet analyte concentration. Additionally, for this configuration, from a flow of 750 μl/min, the total available mass of the analyte is independent of the inlet flow rate, so the only effect of the flow rate will be the deflection on the cantilever and the sensing time.

The application of Computational Fluid Dynamics (CFD) in analyzing fluid behavior within immunoassay cells is crucial for optimizing the design and manufacturing of microfluidic components. Moreover, the use of simulation techniques, as the ones shown in this paper, can play a significant role for the calibration of biosensors by means of the creation of the so-called dose-response curves, which are a key element for the correct operation of these devices, but are normally developed experimentally. This report is integral to developing a multispectral biodetection system named KANAN.PESTI, which is based on Piezoresistive microcantilevers for the detection of different pesticides in aqueous media.

Acknowledgements

The present research work is a Frontiers of Science project identified with number 618306/2020, and was funded by the Mexico's National Council for Humanities, Science, and Technology (CONAHCYT) through FORDECYT-PRONACES, currently program F003.

J. Pérez-Barrera and S. Piedra thank the "Investigadoras e Investigadores por México" from SECIHTI, México.

Conflicts of interest

The authors wish to confirm that there are no known conflicts of interest associated with this publication and there has been no significant financial support for this work that could have influenced its outcome.

1. A. Moulin, S. O'Shea, and M. Welland, Microcantileverbased biosensors, *Ultramicroscopy* **82** (2000) 23, https://doi.org/10.1016/S0304-3991(99)00145-X.
2. A. K. Basu, A. Basu, and S. Bhattacharya, Micro/Nano fabricated cantilever based biosensor platform: A review and recent progress, *Enzyme and Microbial Technology* **139** (2020) 109558, https://doi.org/10.1016/j.enzmictec.2020.109558.
3. A. Mader *et al.*, Discrimination of Escherichia coli Strains using Glycan Cantilever Array Sensors, *Nano Letters* **12** (2012) 420, https://doi.org/10.1021/nl203736u.
4. V. Dauksaite *et al.*, Antibody-based protein detection using piezoresistive cantilever arrays, *Nanotechnology* **18** (2007) 125503, https://doi.org/10.1088/0957-4484/18/12/125503.
5. J. Zhang, et al., Rapid and label-free nanomechanical detection of biomarker transcripts in human RNA, *Nature Nanotechnology* **1** (2006) 214, https://doi.org/10.1038/nnano.2006.134.
6. R. M. R. Pinto, V. Chu, and J. P. Conde, Label-Free Biosensing of DNA in Microfluidics Using Amorphous Silicon Capacitive Micro-Cantilevers, *IEEE Sensors Journal* **20** (2020) 9018, https://doi.org/10.1109/JSEN.2020.2986497.
7. M. Alvarez, et al., Development of nanomechanical biosensors for detection of the pesticide DDT, *Biosensors and Bioelectronics* **18** (2003) 649, https://doi.org/10.1016/S0956-5663(03)00035-6.
8. P. Ray, S. Pandey, and V. Ramgopal Rao, Development of graphene nanoplatelet embedded polymer microcantilever for vapour phase explosive detection applications, *Journal of Applied Physics* **116** (2014), https://doi.org/10.1063/1.4896255.
9. S. Samal *et al.*, Implications of biosensors and nanobiosensors for the eco-friendly detection of public health and agrobased insecticides: *A comprehensive review*, *Heliyon* **9** (2023) e15848, https://doi.org/10.1016/j.heliyon.2023.e15848.
10. M. Z. Ansari *et al.*, Improving sensitivity of piezoresistive microcantilever biosensors using stress concentration region designs, *Journal of Physics D: Applied Physics* **46** (2013) 505501, https://doi.org/10.1088/0022-3727/46/50/505501.
11. I. Sacu and M. Alcı, DESIGN OF A BASIC PIEZORESISTIVE MICROCANTILEVER BIOSENSOR, *IU-Journal of Electrical & Electronics Engineering* **13** (2013) 1641.
12. M. Alvarez and L. M. Lechuga, Microcantilever-based platforms as biosensing tools, *Analyst* **135** (2010) 827, https://doi.org/10.1039/B908503N.
13. J.-Y. Yoon, Introduction to Biosensors: From Electric Circuits to Immunosensors, chap. Wheatstone Bridge, pp. 79-90 (Springer International Publishing Switzerland, 2016), https://doi.org/10.1007/978-3-319-27413-3_5.
14. A. S. Nezhad *et al.*, PDMS Microcantilever-Based Flow Sensor Integration for Lab-on-a-Chip, *IEEE Sensors Journal* **23** (2013) 601, https://doi.org/10.1109/JSEN.2012.2223667.
15. A. Jana *et al.*, Microcantilever mechanics in flowing viscous fluids, *Applied Physics Letters* **23** (2007) 114110, https://doi.org/10.1063/1.2713238.
16. C. Lee *et al.*, Design and characterization of MEMS-based flow-rate and flow-direction microsensor, *Microfluid. Nanofluidics* **23** (2009) 363, https://doi.org/10.1007/s10404-008-0381-6.
17. M.-C. Wu *et al.*, The Effect of Flow Velocity on Microcantilever-Based Biosensors, *Journal of Mechanics* **23** (2007) 353, https://doi.org/10.1017/S1727719100001404.
18. K. Khanafer, K. Vafai, and M. Gaith, Fluid-structure interaction analysis of flow and heat transfer characteristics around a flexible microcantilever in a fluidic cell, *Int. Commun. Heat Mass Transf.* **75** (2016) 315, https://doi.org/10.1016/j.icheatmasstransfer.2016.04.025.
19. S. Elmi, Z. Elmi, and M. Bahrami, Numerical simulation for sensitivity and accuracy enhancement of micro cantilever-based biosensor employing truss structure, *Microsystem Technologies* **25** (2019) 2205, https://doi.org/10.1007/s00542-018-4092-y.
20. A. Saxena *et al.*, Optimization of Newtonian fluid pressure in microcantilever integrated flexible microfluidic channel for healthcare application, *Biomed. Phys. Eng. Express* **10** (2024) 035015, https://doi.org/10.1088/2057-1976/ad3187.
21. S. Vandana *et al.*, Design and Fluid Structure Interaction Analysis of a Micro-channel as Fluid Sensor, *Advanced Engineering Forum* **14** (2015) 46, https://doi.org/10.4028/www.scientific.net/AEF.14.46.
22. B. Rodenberg *et al.*, FEniCS-preCICE: Coupling FEniCS to other simulation software, *Software X* **16** (2021) 100807, https://doi.org/10.1016/j.softx.2021.100807.
23. A. Zanella *et al.*, Towards an open-source framework for Fluid-Structure Interaction using SU2, MBDyn and preCICE, *J. Comput. Appl. Math.* **429** (2023) 115211, https://doi.org/10.1016/j.cam.2023.115211.

24. K. Khanafer and K. Vafai, Microcantilevers in biomedical and thermo/fluid applications, *Frontiers in Heat and Mass Transfer* **1** (2010) 023004, https://doi.org/10.5098/hmt.v1.2.3004.

25. K. Khanafer and K. Vafai, Geometrical and flow configurations for enhanced microcantilever detection within a fluidic cell, *Int. J. Heat Mass Transf.* **48** (2005) 2886, https://doi.org/10.1016/j.ijheatmasstransfer.2004.11.021.

26. A. Tafuni and I. Sahin, Hydrodynamic loads on vibrating cantilevers under a free Surface in viscous fluids with SPH, In In Proc. ASME 2013 International Mechanical Engineering Congress & Exposition (2013) pp. IMECE2013-63792-1-8.

27. H.-J. Bungartz *et al.*, preCICE - A fully parallel library for multi-physics surface coupling, *Computers & Fluids* **141** (2016) 250, https://doi.org/10.1016/j.compfluid.2016.04.003.

28. H. G. Weller *et al.*, A tensorial approach to computational continuum mechanics using object-oriented techniques, *Computers in Physics* **12** (1998) 620, https://doi.org/10.1063/1.168744.

29. OpenFOAM.com, OpenFOAM - The Open Source CFD Toolbox-User's Guide (2018), https://www.openfoam.com/documentation/user-guide.

30. D. Arndt *et al.*, The deal.II finite element library: Design, features, and insights, *Computers & Mathematics with Applications* **81** (2021) 407, https://doi.org/10.1016/j.camwa.2020.02.022.

31. D. Arndt *et al.*, The deal.II Library, Version 9.4, *Journal of Numerical Mathematics* **30** (2022) 231, https://doi.org/10.1515/jnma-2022-0054